PHYSICAL REVIEW B **81**, 245412 (2010)

Transport between twisted graphene layers

R. Bistritzer and A. H. MacDonald
Department of Physics, The University of Texas at Austin, Austin, Texas 78712, USA
(Received 5 April 2010; revised manuscript received 23 May 2010; published 8 June 2010)

Commensurate-incommensurate transitions are ubiquitous in physics and are often accompanied by intriguing phenomena. In few-layer graphene (FLG) systems, commensurability between honeycomb lattices on adjacent layers is regulated by their relative orientation angle θ, which is in turn dependent on sample preparation procedures. Because incommensurability suppresses interlayer hybridization, it is often claimed that graphene layers can be electrically isolated by a relative twist, even though they are vertically separated by a fraction of a nanometer. We present a theory of interlayer transport in FLG systems which reveals a richer picture in which the specific conductance depends sensitively on θ, single-layer Bloch-state lifetime, in-plane magnetic field, and bias voltage. We find that linear and differential conductances are generally large and negative near commensurate values of θ, and small and positive otherwise. We show that accounting for interlayer coupling may be essential for describing transport in FLG despite its physically insignificant effect on the band structure of the system.

DOI: 10.1103/PhysRevB.81.245412 PACS number(s): 72.80.Vp, 73.22.Pr, 73.40.−c

I. INTRODUCTION

Experimental advances in the fabrication of graphene-based structures[1,2] have now provided researchers with a multitude of systems that have strikingly distinct electronic properties. By engineering the substrate underlying exfoliated samples,[3–5] identifying exfoliated fragments with folds[6] or controlling epitaxial growth conditions,[7–9] the size and shape of the honeycomb lattice arrays[10,11] and the number of graphene layers and their orientations can all be varied. This structural diversity nourishes hopes for a future carbon-based electronics[12] with band-structure and transport characteristics that can be tailored for different types of applications.

Few-layer graphene (FLG) has advantages over single-layer graphene because it has a larger current-carrying capacity and because its electronic properties are sensitive to more engineerable system parameters.[13] In nature it appears in a variety of stacking arrangements, the most common being Bernal and rhombohedral sequences which form three-dimensional lattices. It has been understood for some time[14] that in graphite θ can depart from Bernal values. With some interesting exceptions,[5,15] most recent studies of interlayer twists in FLG have focused on samples grown on SiC.[16] In particular, Hass *et al.* have demonstrated that orientational disorder is normally present in carbon-face SiC epitaxial FLG samples.[17] The present work is motivated primarily by the need to achieve a more complete understanding of transport in these graphitic nanostructures, which currently appear to provide the most promising platform for applications.

In a bilayer system, the relative rotation angle θ can be classified as either commensurate or incommensurate.[18] In the former case the misaligned bilayer system still forms a crystal, albeit one with larger lattice vectors and more than four atoms per unit cell. Commensurability occurs at a countably infinite set of orientations but the probability that a randomly selected orientation angle is commensurate vanishes. The energy bands of commensurate twisted multilayers disperse approximately linearly with momentum,[19–21] except at energies very close to the Dirac point. However, the Dirac velocity is reduced compared to that of a single-layer system especially for rotation angles close to 0° or 60°.[15,20] The linear Dirac-type dispersion contrasts with the approximately quadratic dispersion found in a Bernal stacked bilayer system.[22] Incommensurate bilayers are not crystalline[23] and therefore their electronic properties cannot be analyzed using Bloch's theorem.

Here we develop a theory for the vertical transport properties of twisted FLG samples which is valid in the incoherent transport limit.[24] We show that the specific linear conductance between misaligned layers is enhanced over a small but finite range of twist angles near those that produce relatively short-period commensurate structures, that the conductance peak angles shift with in-plane magnetic field $B_{\parallel}$, and that the peaks become narrower and stronger when the isolated-layer Bloch-state lifetime τ increases. The differential conductivity tends to be negative near commensurate conductance peaks and positive otherwise. Typical theoretical results for the dependence of the interlayer equilibration rate on θ are presented in Fig. 1. In the following we first explain the analysis which supports these statements and then discuss some implications for FLG electronics.

II. INTERLAYER CURRENT

Studies of transport between weakly coupled two-dimensional (2D) electron systems have a long history[25,26] in semiconductor heterojunctions systems. In that case epitaxial tunnel barriers are responsible for nearly perfect 2D momentum conservation, which then helps to make vertical transport a powerful probe of electronic properties. Our theory of vertical transport in FLG is similar to the successful semiconductor heterojunction theory.[25] We derive an expression for tunneling current I vs bias voltage V by using a π-orbital tight-binding model, approximating interlayer hopping processes at leading order in perturbation theory, and accounting for the inevitable presence of a finite disorder potential which limits the life times of Bloch states in each layer. These steps lead to

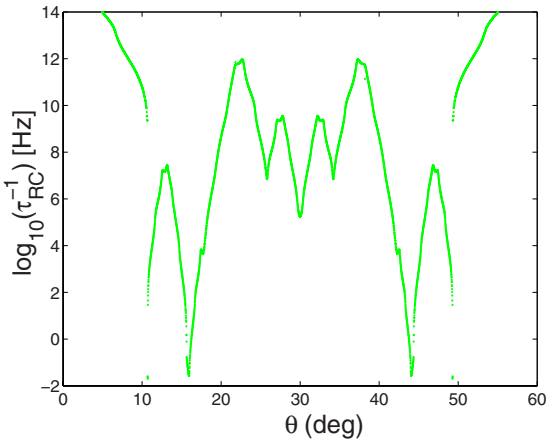

FIG. 1. (Color online) Interlayer (RC) equilibration rate as a function of twist angle θ. These results were calculated for two layers with equal carrier densities ($n=5\times10^{12}$ cm^{-2}) and $\epsilon_F\tau=3$, where ϵ_F is the Fermi energy and τ is the isolated-layer Bloch-state lifetime. The relaxation rate is dominated by separate features that appear near every commensurate angle but differ in strength by many orders of magnitude. The tails of individual features have been cut off in this plot in order to reveal weaker features that will emerge in more ideal bilayers. Except near $\theta=0°,60°$, the equilibration rate is surprisingly slow for two layers separated by an atomic length scale. The six conduction peaks in the figure correspond to the commensurate angles near 13.2°, 21.8°, 27.8°, 32.2°, 38.2°, and 46.8°.

$$I(\theta) = eg_s \int \frac{d\omega}{2\pi}[n_{F1}(\omega) - n_{F2}(\omega + eV)] \times \sum_{\mathbf{kp}'} |T^{\alpha\beta}_{\mathbf{kp}'}|^2 A_{1\alpha}(\mathbf{k},\omega) A_{2\beta}(\mathbf{p}',\omega+eV), \quad (1)$$

where $g_s=2$ accounts for spin degeneracy, $A_{i\alpha}(\mathbf{k},\omega)$ is the spectral function for band α and layer i, n_{Fi} is the Fermi distribution function for layer i, and $T^{\alpha\beta}_{\mathbf{kp}'}$ is the tunneling matrix element between isolated-layer Bloch states with band and crystal momentum labels, $|\mathbf{k}\alpha\rangle$ and $|\mathbf{p}'\beta\rangle$. The sums over $\mathbf{k}$ and $\mathbf{p}'$ may be taken over the unrotated and rotated Brillouin zones, respectively. We derive Eq. (1) in Appendix B, where we justify its neglect of disorder vertex corrections. In our calculations, A is approximated by a Lorentzian function with full width half maximum $\hbar/\tau$ centered on the band energy $\epsilon_{i\alpha}(\mathbf{k})$. (Hereafter $\hbar=1$ and length is measured in units of $a_c=1.42$ Å, the carbon-carbon distance in graphene.) Equation (1) is valid in the weak tunneling regime in which T is smaller than lifetime broadening $1/\tau$, allowing coherent tunneling processes to be neglected. This condition is satisfied in typical samples except at rotation angles very close to 0° or 60°.

In a twisted bilayer system the tunneling matrix element depends strongly on the relative orientation of the two graphene sheets. The honeycomb lattice vectors of the rotated layer $\mathbf{R}'$ are related to those of the unrotated layer $\mathbf{R}$ by $\mathbf{R}'=M(\theta)\mathbf{R}+\mathbf{d}$. Here M is the transformation matrix for rotations in the lattice plane and $\mathbf{d}$ is a translation vector. Corresponding rotations occur in reciprocal space so that $\epsilon_{1\alpha}(\mathbf{p})=\epsilon_{2\alpha}(\mathbf{p}')$ when $\mathbf{p}'=M(\theta)\mathbf{p}$. Commensurability is determined only by M, but linear translations of one layer relative to the other do modify T, and hence the tunneling current.

The magnitude of T depends on the π-orbital interlayer hopping amplitudes of our tight-binding model which we estimate using a simple two-center approximation scheme explained in Appendix A. We find that

$$T^{\alpha\beta}_{\mathbf{kp}'} = \frac{1}{\Omega_0}\sum_{s,\bar{s}} (a^{(\alpha)}_{\mathbf{k}s})^\star a^{(\beta)}_{\mathbf{p}\bar{s}} \sum_{\mathbf{G_1G_2}} t_{\mathbf{k}+\mathbf{G_1}} e^{-i(\mathbf{k}+\mathbf{G_1})\cdot\mathbf{d}} \times e^{i\mathbf{G_1}\cdot\tau_s} e^{-i\mathbf{G_2}\cdot\tau_{\bar{s}}} \delta_{\mathbf{k}+\mathbf{G_1},\mathbf{p}'+\mathbf{G}'_2}, \quad (2)$$

where Ω_0 is the area of a unit cell. Here $\mathbf{G_1}$ and $\mathbf{G_2}$ are summed over reciprocal-lattice vectors, primed wave vectors are rotated, s and $\bar{s}$ label the two triangular honeycomb sublattices centered at positions $\tau_\mathbf{s}$, and $a^{(\alpha)}_{\mathbf{k}s}$ is the sublattice projection of the $|\mathbf{k}\alpha\rangle$ Bloch state in the unrotated layer. In Eq. (2), which is derived in Appendix A, $t_\mathbf{k}$ is the 2D Fourier transform of the finite-range interlayer hopping amplitude. As we will explain, the interlayer conductance and the layer equilibration rate are proportional to $|t_\mathbf{k}|^2$ values for $|\mathbf{k}|$'s that are larger than the Brillouin-zone scale (except for $\theta \approx 0°, 60°$). Because the interlayer distance is already larger than the carbon-carbon distance within a layer, these $|t_\mathbf{k}|^2$ values tend to be both extremely small and extraordinarily sensitive to details of the interlayer tunneling model that are otherwise inconsequential.

We have used Eqs. (1) and (2) to evaluate interlayer currents as a function of rotation angle θ, carrier density, bias voltage, and disorder strength. Since for typical electronic densities the temperature T is much less than the Fermi temperature we focus on $T=0$ hereafter.

III. LINEAR CONDUCTANCE

It is helpful to first focus on the linear conductance

$$G(\theta) = \frac{e^2 g_s}{2\pi}\sum_{\mathbf{kp}'} |T^{\alpha\beta}_{\mathbf{kp}'}|^2 A_{1\alpha}(\mathbf{k},\epsilon_F) A_{2\beta}(\mathbf{p}',\epsilon_F). \quad (3)$$

The equilibration rate plotted in Fig. 1 was obtained by viewing the bilayer as a leaky capacitor and ignoring any screening by graphene σ orbitals. This model yields an RC circuit with time constant τ_{RC} related to the conductance by $G/\mathcal{A} = 0.027\tau^{-1}_{RC}$, where $\mathcal{A}$ is the layer area in m^2, G is measured in siemens, and τ_{RC} in seconds. Apart from a change in scale, Fig. 1 can then be viewed as a plot of the interlayer conductance. We find that the tunneling conductance increases abruptly near commensurate angles, that the height of the peaks scales linearly with $\epsilon_F\tau$ (for $\epsilon_F\tau>1$), and that the peaks narrow as τ increases. The discontinuous jumps of $\log(G)$ in Fig. 1 are artificial and result from a numerical procedure in which momenta $\mathbf{k}$ and $\mathbf{p}'$ in Eq. (3) are restricted to the vicinity of the Fermi energy. This procedure suppresses the tails of all commensurate features, allowing more minor features to be revealed. In practice the conduction tails corresponding to highly commensurate structures will dominate G over a range of angles that depends on τ.

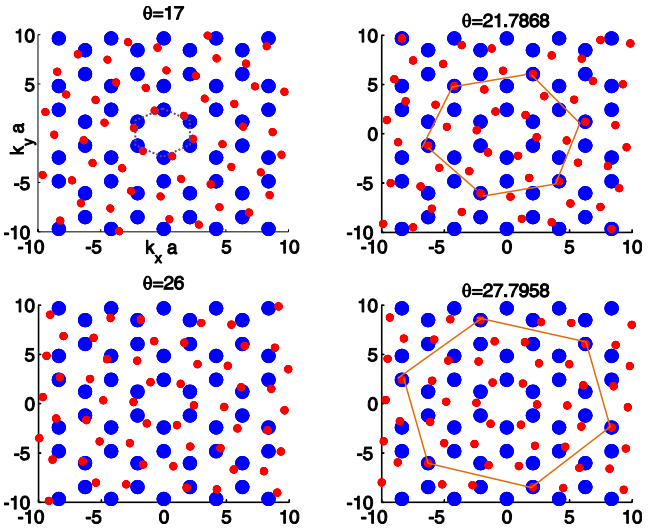

FIG. 2. (Color online) Fermi circles in an extended-zone scheme. The blue(large) and red(small) circles correspond to the Fermi circles in the unrotated and rotated layers, respectively. The area enclosed by the circles is proportional to the carrier density. Conductance contributions occur when the Fermi circles intersect and are much larger when the intersection occurs closer to the origin of momentum space. The Brillouin-zone boundary connects the centers of the inner shell of blue circles as indicated by the dashed lines in the $\theta=17°$ panel.

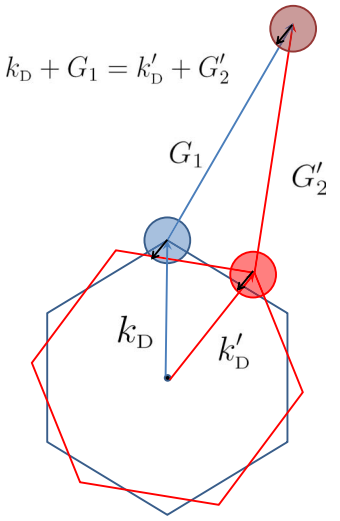

FIG. 3. (Color online) Nesting of Dirac cones at commensurability. For commensurate rotation angles every momenta state on the rotated Fermi circle is mapped onto a momenta state of an unrotated Fermi circle.

Limited by computational power we considered $\tau^{-1} \approx 75$ meV in Fig. 1, however, in epitaxial graphene the lifetime can be more than an order of magnitude longer.[27] An accurate theory of the conduction-peak tails would require a reliable theory of the isolated-layer spectral-function tails.

Why is the tunneling conductance enhanced at commensurate rotation angles? To understand the relation between interlayer current and commensurability it is illuminating to plot the Fermi surfaces of both layers, periodically extended in momentum space by adding reciprocal-lattice vectors to the crystal momenta of the electrons. As we see in Eq. (2), allowed interlayer tunneling processes are diagonal in this generalized momentum. The left panels in Fig. 2 correspond to the incommensurate rotation angles $\theta=17°, 26°$ whereas the right panels correspond to the commensurate angles near $\theta=21.8°, 27.8°$. We use different Fermi surfaces' sizes for clarity; similar considerations apply independent of the sign or magnitude of the carrier density ratio. The key feature to notice in these plots is that at commensurate rotation angles some Fermi spheres overlap. Overlaps of circles centered on the extended Dirac points, *always* accompany commensurate real-space structures because the set of extended Dirac points forms a momentum-space honeycomb lattice that differs from the real-space honeycomb lattice only by a scale factor and by a rotation. If overlaps occur in real space, they also occur in momentum space. Notice that this property holds only when the Brillouin-zone corners are extended to fill momentum space; if the Dirac point occurred elsewhere in the isolated-layer Brillouin zone, the dependence of interlayer conductance on θ would be quite different.

The overlap of extended Dirac points does not fully explain the conductance peaks at finite density since Fermi energy states at finite carrier density are displaced from the Dirac point. The nesting between Fermi surfaces alluded to in Fig. 2 actually depends not only on commensurability but also on the fact that for typical carrier densities the Fermi surface is well approximated by a circle centered on the Brillouin-zone corners. For equal densities then, matching Dirac points implies complete Fermi-surface nesting (see Fig. 3). When the two layers have different densities, the peak conductance will not occur at the nesting angle; instead the conductance will have a double-peak structure with features offset to both sides of the commensurate angle.

Commensurate rotation angles can be classified as either intervalley or intravalley. In the former the two Dirac points k_D and k'_D that coincide in the extended momentum picture are associated with different valleys (in the aligned bilayer) whereas for intravalley rotation angles they belong to the same valley. An intervalley commensurate rotation is illustrated in Fig. 3.

Away from commensurate angles the energy difference between states which have the same extended momentum is typically much larger than the Fermi energy, and the spectral-function width $1/\tau$ (see left panels of Fig. 2). The conductance is therefore very small away from the commensurate-angle peaks. The Dirac-type linear spectrum of an ideal commensurately twisted bilayer does not, as is commonly stated, indicate that the ideal twisted layers are decoupled. At commensurate angles the perfect-crystal wave functions near the Dirac point are in fact coherent equal-weight contributions from the two layers. In the limit of large in-plane Bloch-state lifetimes, the conductance becomes very large and eventually the incoherent transport picture will fail.

As we have explained, vertical transport at commensurability is dominated by processes in which an electron tunnels from a momentum near a Dirac point of one layer, to a momentum that is the same distance from a Dirac point of the other layer. Since carrier densities per unit cell are always small, we can replace $t_{\mathbf{k}+\mathbf{G}}$ in Eq. (2) by $t_{\mathbf{k}_D+\mathbf{G}}$, where $\mathbf{k}_D$ is

the Dirac point momentum. We then find that the conductance peak can be expressed as

$$G \approx R_{cc}(\theta_c, \mathbf{d}) \times \mathcal{F}(\epsilon_F \tau). \tag{4}$$

Here θ_c is the commensurate orientation,

$$\mathcal{F} = \sum_{\mathbf{k}} A_1(k, \epsilon_F) A_1(k, \epsilon_F)$$

$$= \frac{\mathcal{A}}{2\pi v^2}[2 + 2\pi\epsilon_F\tau + 4\epsilon_F\tau \arctan(2\epsilon_F\tau)] \tag{5}$$

is the phase-space factor which is identical to the one that appears in the theory of coupled quantum wells,[25] and

$$R_{\alpha\beta} = \int \frac{d\theta_k}{2\pi} |T^{\alpha\beta}(\theta_k)|^2 \tag{6}$$

is the geometric matrix that depends on the relative alignment of the two layers. Strictly speaking, the interlayer current is a sum of four distinct processes, associated with the four entries of $R_{\alpha\beta}$, in which an electron from band α in one layer tunnels to band β in the other layer. However, for the linear conductance of an electron doped system R_{cc} dominates G.

The geometric matrix $R(\theta_c, \mathbf{d})$ depends mainly on the value of $t_{|\mathbf{k_D}+\mathbf{G}|}$ at which the extended Dirac points overlap (see Fig. 2). For pure rotations R can be calculated analytically. We defer the details to Appendix C where we find that

$$R_{cc}(\theta_c, \mathbf{d} = 0) = \frac{E_g^2(\theta_c)}{16} \times \begin{cases} 4\cos^2(\phi - \theta_c/2) & \theta_c \in S \\ 1 & \theta_c \in D \end{cases}, \tag{7}$$

where $\theta_c \in S$ correspond to intravalley commensurate angles and $\theta_c \in D$ to their intervalley counterparts. The angle ϕ assumes one of the three values $0, \pm 60$ depending on θ_c, e.g., $\phi(0°)=0$, $\phi(27.8°)=60°$, and $\phi(38.2°)=-60°$. As we show in Sec. V the tunneling amplitude in Eq. (6) is related to the energy gap E_g (the difference between the highest conduction band and lowest valance band) at the Dirac point. It then follows from Eq. (4) that

$$G(\theta_c, \mathbf{d} = 0) = \mathcal{A} g_s g_v \frac{e^2}{\hbar} \frac{\epsilon_F \tau}{\pi v^2} R_{cc}(\theta_c, \mathbf{d} = 0) \tag{8}$$

for $\epsilon_F\tau > 1$, where $g_v = 2$ accounts for the valley degeneracy. We numerically verify that the conductance changes only by a factor of order unity as $\mathbf{d}$ is varied across the unit cell (see Fig. 4). Equation (8) therefore provides a good estimate for G regardless of the relative translation between the two layers. Interestingly, the ratio

$$\Delta G(\theta_c) \equiv \frac{G^S(\theta_c, d = 0)}{G^D(60° - \theta_c, d = 0)} = 4\cos^2\left(\phi - \frac{\theta_c}{2}\right) \tag{9}$$

depends only on the twist angle. For example, $\Delta G(27.8°) = 1.94$ in accord with the numerical results depicted in Fig. 4.

Electronic-structure calculations for ideal commensurate bilayers demonstrate that E_g decreases very rapidly as the number of atoms per unit cell increases.[18] $E_g = 780$ meV for a unit cell of four atoms, and already less that 1 meV for a unit cell of 100 atoms. It is therefore plausible that conductance tails that correspond to the few lowest-order commensurate angles (e.g., $\theta_c = 0°, 21.8°, 27.8°, 32.2°, 38.2°, 60°$) will dominate G at every rotation angle. Equation (8) should therefore be interpreted as a lower bound for the conductance at higher-order commensurate θ_c's.

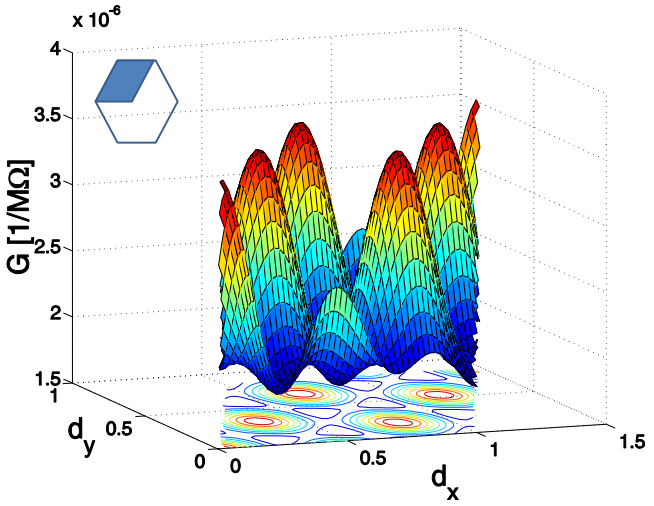

FIG. 4. (Color online) Dependence of conductance per unit cell G on translation $\mathbf{d}$ for $\theta = 27.8°$, $\epsilon_F\tau = 3$, and $n = 5 \times 10^{12}$ cm^{-2}.

Commensurability depends only on the relative rotation of the two graphene layers. Nevertheless linear translation of one layer with respect to the other will change the tunneling current. In Fig. 4 the conductance at $\theta = 27.8°$ is plotted as a function of $\mathbf{d}$ for a bilayer with $n = 5 \times 10^{12}$ cm^{-2} in each layer and $\epsilon_F\tau = 3$. The dependence of the tunneling current on $\mathbf{d}$ is periodic in the lattice vectors of both layers.

As illustrated in Fig. 1 the conductance peaks appear symmetrically around $\theta = 30°$ but the height of a peak with $\theta < 30°$ does not necessarily equal the height of the corresponding peak at $\theta' = 60° - \theta$. In fact, the relative height of the two peaks depends on $\mathbf{d}$. An AA stacking sequence can be transformed to Bernal stacking either by a pure rotation with $\theta = 60°$ or by a translation with $\mathbf{d} = (1, 0)$. Since the latter transformation does not influence commensurability any commensurate angle θ_c of the AA stacked bilayer is a commensurate angle of the Bernal stacked bilayer. The conductance peaks then lie symmetrically with respect to $\theta = 30°$ since if θ is commensurate so is its inverse.

IV. NONLINEAR *I-V*

We now turn to the nonlinear *I-V* of twisted bilayer graphene. At zero temperature

$$I(\theta, V) = \frac{e g_s}{2\pi} \sum_{kp} |T_{kp'}|^2 \int_{\epsilon_F - eV}^{\epsilon_F} d\omega A_1(k, \omega) A_2(p', \omega + eV). \tag{10}$$

We numerically find that the *I-V* curves at commensurate and incommensurate angles are drastically different. At relatively small bias voltage the currents corresponding to commensu-

rate angles are several orders of magnitude larger than their incommensurate counterparts. On the other hand negative differential conductances invariably appear at commensurate angles whereas dI/dV tends to be small and positive at incommensurate angles.

In classic tunneling experiments, a bias voltage induces an electric potential difference between the layers. Total-energy conservation then implies kinetic energy changes equal to eV upon tunneling. Since, as we have explained, the allowed tunneling processes at commensurate angles are between states with the same kinetic-energy bias voltages tend to decrease tunneling currents. Following the same approximations that led to Eq. (4) we can capture this effect mathematically by expressing the interlayer current in product form

$$I = \frac{e}{2\pi}\sum_{\alpha\beta} R_{\alpha\beta}(\theta,\mathbf{d})\int_{-\infty}^{\infty} d\omega[n_F(\omega) - n_F(\omega+V)] \times \sum_{\mathbf{K}} A_\alpha(k,\omega)A_\beta(k,\omega+eV). \tag{11}$$

In Eq. (11) we have allowed for both intraband and interband tunneling at large biases. As long as $eV < \epsilon_F$ tunneling between conduction bands dominate I when both layers are n type. In this intermediate nonlinear regime the two Lorentzian shaped spectral functions in Eq. (11) overlap only weakly and

$$I(\theta_c,\mathbf{d}) \approx G(\theta_c,\mathbf{d})\frac{V}{1+(eV\tau)^2} \tag{12}$$

for $\epsilon_F\tau > 1$. Negative differential conductance occurs when $eV\tau > 1$. For incommensurate twist angles, crystal momenta conservation cannot be sustained at the Fermi surface. Increasing V unblocks processes in which tunneling occurs between states with different kinetic energies and leads to a slow increase in the tunneling current with a complex dependence on $t_{\mathbf{q}}$ and $\hbar/\tau$. For $eV > \epsilon_F$, the current increases monotonically with V for both commensurate and incommensurate twist angles. The commensurate tunneling current has a sharp rise at $eV = 2\epsilon_F$ due to momentum conserving processes allowed at high bias voltage in which a valence-band electron in one layer tunnels to the conduction band of the opposite layer. For commensurate angles it follows from Eq. (11) that these interband processes eventually dominate the tunneling current and that

$$I \approx \frac{e^2}{4v^2}R_{vc}\Theta(V-2\epsilon_F)V \tag{13}$$

to leading order in $1/V\tau$. Here Θ is the Heaviside step function. The finite-temperature corrections to Eqs. (12) and (13) are exponentially small in T/ϵ_F. For $\mathbf{d}=0$ we find in Appendix C that

$$R_{vc}(\theta_c,\mathbf{d}=0) = \frac{E_g^2(\theta_c)}{16}\times\begin{cases} 4\sin^2(\phi-\theta_c/2) & \theta_c \in S \\ 1 & \theta_c \in D. \end{cases} \tag{14}$$

V. ENERGY BANDS FOR TWISTED BILAYERS AT COMMENSURABILITY

In the vicinity of the Dirac point the Hamiltonian for the twisted bilayer is well approximated by

$$H = \begin{pmatrix} H_k & T \\ T^\dagger & H_k(\theta) \end{pmatrix}. \tag{15}$$

Here H_k is the intralayer Hamiltonian and T is the 2×2 interlayer tunneling matrix. For commensurate rotation angles we show in Appendix C that

$$T^D = e^{i(2\theta_k+\theta_c)}|a|I \tag{16}$$

and that

$$T^S = 2e^{i(\phi+\theta_c/2)}|a|\begin{pmatrix} \cos\left(\phi-\frac{\theta_c}{2}\right) & -i\sin\left(\phi-\frac{\theta_c}{2}\right) \\ -i\sin\left(\phi-\frac{\theta_c}{2}\right) & \cos\left(\phi-\frac{\theta_c}{2}\right) \end{pmatrix} \tag{17}$$

in the eigenstate representation. Here T^S and T^D correspond, respectively, to intravalley (S=same) and intervalley (D=different) rotation angles. The intralayer Hamiltonian $H_k(\theta)=\epsilon_k\sigma_z$ is independent of the rotation angle in the eigenstate basis. It then follows form Eq. (15) that the four nondegenerate bands corresponding to bilayers with intervalley rotation angles are

$$E_k^D = \pm\sqrt{\epsilon_k^2 + 2|a|^2 \pm 2\sqrt{\epsilon_k^2|a|^2+|a|^4}}. \tag{18}$$

At low energies $\epsilon_k \ll a$

$$E_{k1}^D = \pm\frac{k^2}{2m^\star}, \quad E_{k2}^D = \pm 2|a| \pm \frac{k^2}{2m^\star}, \tag{19}$$

where $m^\star = |a|/v^2$. For the intravalley rotations

$$E_k^S = \pm\sqrt{\epsilon_k^2 + 4|a|^2 \pm 4|a|\epsilon_k\cos(\phi-\theta_c/2)}. \tag{20}$$

At low energies $\epsilon_k \ll a$

$$E_k^S = \pm 2|a| \pm v^\star k, \tag{21}$$

where $v^\star = v\cos(\phi-\theta_c/2)$. Deviations from expressions (16) and (17) for T result in trigonal warping in an AB bilayer system. More elaborate studies of the spectrum are needed to determine whether such effects are important in a rotated bilayer system as well. Similar results were recently obtained by Mele.[28]

For either type of rotation $E_g = 4|a|$. As mentioned above, E_g is extremely small for all but the most commensurate structures. It is not surprising then that band-structure experiments seem to indicate that FLG systems act as independent graphene layers. Nevertheless, as we explain in the next section, accounting for the interlayer coupling may be essential for describing the transport in FLG systems.

VI. DISCUSSION

One application of our theory is to assess whether or not twisted graphene layers are effectively isolated from an elec-

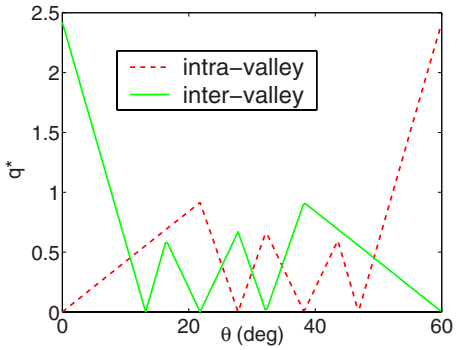

FIG. 5. (Color online) The minimum separation between extended Dirac points $q^\star$ as a function of rotation angle θ.

trical point of view. The equilibration time between layers that are spatially uniform but out of equilibrium is plotted in Fig. 1 and is very long compared to characteristic electronic time scales for rotation angles far from important commensurabilities (near 10°, for example). The steady-state equilibration length between separately contacted layers can be estimated by equating interlayer conductances, which are proportional to sample area, with the intralayer conductance per square. For the commensurate angle $\theta_c=21.8°$, for example, the sample area at which they are identical is approximately 0.04 μm^2. As evident from Fig. 1, the corresponding areas for small rotation angles near the *AA* and *AB* stacking sequences are even smaller. For small rotation angles, the two layers are therefore strongly coupled.

The interlayer conductance $G(\theta)$ is peaked whenever any extended Fermi-surface overlap occurs at reasonably small reciprocal-lattice vectors. The degree of overlap can be parameterized by $q^\star$, the minimum separation between extended Dirac points of the rotated and unrotated layers for a reciprocal-lattice vector truncation chosen to reflect the scale on which $t_{\mathbf{q}}$ falls off. For a clean system, tunneling conductance at equal density is appreciable as long as $q^\star \approx |\theta - \theta_c||\mathbf{k}+\mathbf{G}| < 2k_F$. Because $2k_F$ in FLG electronic systems is always small compared to reciprocal-lattice vector scales, the conductance peaks are invariably sharp when plotted as a function of θ. As an example $q^\star \approx 6.39|\theta - \theta_c|$ in the vicinity of $\theta_c=27.8°$ for the reciprocal-lattice vector illustrated in Fig. 2. In Fig. 5, $q^\star$, minimized over the first two G shells, is plotted as a function of angle. Overlap between the Fermi spheres of the two layers will therefore persist over the angle range for which $q^\star$ is smaller than $2k_F$.

When the densities differ, Fermi circles in different layers begin to overlap near $\theta=\theta_c$ only after a momentum-space relative shift $\mathbf{Q}$ equal in magnitude to the difference of the two Fermi wave vectors. As in semiconductor double wells,[25,26,29] a shift $\mathbf{Q}=\hat{\mathbf{z}}\times\hat{\mathbf{e}}d_\perp/l_H^2$, where l_H is the magnetic length, can be accomplished in a bilayer with layer separation $d_\perp$ by applying an in-plane magnetic field $B_\parallel\hat{\mathbf{e}}$. For graphene bilayers, however, a relative momentum-space shift can also be achieved by rotation, as is clear from Fig. 2. For small departures from commensurability $\mathbf{Q}\approx(\theta-\theta_c)\hat{z}\times(\mathbf{k_D}+\mathbf{G})$. For equal densities, both rotations and in-plane fields dramatically suppress the conductance peak when $vQ \geq 1/\tau$, where v is the band velocity of graphene. For example, for $n=4\times10^{12}$ cm^{-2} and $\tau=50$ fs,[6] the conductance peak should nearly completely disappear at 0.15 T. FLG should therefore provide a palette on which gate voltages, in-plane magnetic fields, and rotations can be mixed to produce a rainbow of interrelated and extraordinarily strong magnetic field and strain-sensitive resistance effects.

The extension of our theory to FLG is straightforward in the linear regime. In the simplest case each layer is rotated with respect to its neighbors sufficiently to drive the system into an incoherent transport regime. The weak links between layers then act like classical resistors which appear in series in vertical transport. The resistance of each link depends on the rotation angle between layers and on the densities in both layers. We anticipate a very rich and complex behavior of FLG in the nonlinear regime. The negative differential conductivities are likely to give rise to steady-state multistability and to chaotic temporal response, as occurs in semiconductor multiple-quantum-well systems.[31] A more complicated scenario could arise in turbostratic graphene. There the entire layered structure is composed of a set of coherent multilayer substructures, characterized by either a Bernal or an *AA* stacking sequence. Weak links which play a dominant role in limiting vertical conductance appear due to occasional twists. The calculations for the resistance of each twisted interface closely follow those outlined above for the two-layer case when supplemented by a band index for the various 2D energy bands of a coherent substructure.

Finally we remark that the extraordinary sensitivity of the tunneling conductance to the twist angle found here suggests that misaligned graphene bilayers might be useful as ultrasensitive strain gauges or pressure sensors[32] which are widely used in biological, mechanical, and optical systems.

ACKNOWLEDGMENTS

The authors acknowledge support from CERA, SWAN, and the Welch Foundation and helpful conversations with W. de Heer, R. Duine, P. First, D. Goldhaber-Gordon, R. Lifshitz, and E. Tutuc.

APPENDIX A: THE TUNNELING MATRIX ELEMENTS

The interlayer hopping terms in a π-band tight-binding Hamiltonian for twisted graphene bilayers depend in general on the positions of all carbon atoms. Our analysis of interlayer conductance and equilibration is based on a simple two-center model in which the interlayer hopping parameter between two sites, $t(\mathbf{r})$, depends only on the planar projection of their separation $\mathbf{r}$. In the main text we used an equation, derived below, which relates the interlayer hopping amplitudes of twisted bilayers to $t_{\mathbf{q}}$, the two-dimensional Fourier transform of $t(\mathbf{r})$.

One strategy which can be used to estimate $t(\mathbf{r})$ is to assume functional forms for the distance dependence of the Slater-Koster $t_{pp\sigma}$ and $t_{pp\pi}$ hopping functions,[33] and then fit them to accurately known parameters of untwisted bilayers. We have explored this approach, following the procedures adopted in Refs. 18 and 30 but have concluded that it tends to underestimate hopping amplitudes near the Dirac points of

twisted bilayers. We have therefore decided to obtain numerical estimates by directly fitting an *ansatz* for $t_{\mathbf{q}}$ to obtain

$$t_{\mathbf{q}} = t_0 e^{-\alpha(qd_\perp)^\gamma}, \tag{A1}$$

where $t_0=2$ eV Å^2, $\alpha=0.13$, $\gamma=1.25$, and $d_\perp=3.34$ Å is the distance between the layers. The value used for t_0 is the average of values implied by the models in Refs. 18 and 30. Since t_0 is the sum of all interlayer hopping parameters, it should be estimated reliably by any parameterization that uses accurate values for the largest hopping parameters. We fix α and γ so that the values of the ideal bilayer gaps are accurate for the lowest-order commensurate structures. These are proportional to t_{k_D} ($\theta=0°$ and $\theta=60°$) and $t_{6.4/a_c}$ ($\theta=21.8°$ and $\theta=38.2°$), where $a_c=1.42$ Å is the carbon-carbon distance in single-layer graphene. See details in Appendix C below. We fit the energy gaps to values extracted from the *ab initio* calculations by Shallcross *et al.*[18] Note that these values of $t_{\mathbf{q}}$ characterize short-distance roughness in the interlayer hopping landscape which survives Fourier transformation at large wave vectors, are not simply related to typical interlayer hopping strengths. The energy gaps that we obtain at $\theta=21.8°$ using the real-space parameterizations of $t_{pp\sigma}(r)$ and $t_{pp\pi}(r)$ in Refs. 18 and 30 are both substantially smaller than the *ab initio* gaps of Shallcross *et al.*[18]

We now derive the expression for the hopping amplitude between Bloch states in twisted bilayers that is used in the main text. The Bloch state in layer j with crystal momentum $\mathbf{k}$ and band index α can be written as

$$|\Psi_{\mathbf{k}\alpha}^{(j)}\rangle = a_{\mathbf{k}\mathrm{A}}^{j\alpha}|\psi_{\mathbf{k}\mathrm{A}}^{(j)}\rangle + a_{\mathbf{k}\mathrm{B}}^{j\alpha}|\psi_{\mathbf{k}\mathrm{B}}^{(j)}\rangle, \tag{A2}$$

where A and B label the two triangular honeycomb sublattices,

$$\begin{pmatrix} a_{\mathbf{k}\mathrm{A}}^{1\alpha} \\ a_{\mathbf{k}\mathrm{B}}^{1\alpha} \end{pmatrix} = \frac{1}{\sqrt{2}} \begin{pmatrix} e^{i\Theta_{\mathbf{k}}} \\ \alpha \end{pmatrix}, \tag{A3}$$

and $\Theta_{\mathbf{k}}$ is the phase of the intersublattice hopping term in the single-layer tight-binding model. For nearest neighbor hopping within the planes $\Theta_{\mathbf{k}}=\arg(\Sigma_j e^{i\mathbf{k}\cdot\delta_j})$, where the δ_j are the three vectors connecting an atom with its nearest neighbors. The Bloch-state projection on sublattice s is

$$|\psi_{\mathbf{k}s}^{(1)}\rangle = \frac{1}{\sqrt{N}} \sum_{\mathbf{R}} e^{i\mathbf{k}(\mathbf{R}+\tau_s)}|\tau_s+\mathbf{R}\rangle, \tag{A4}$$

where $|\tau_s+\mathbf{R}\rangle$ is a site-representation basis function of the tight-binding model. In Eq. (A4) $\mathbf{R}$ is a triangular lattice vector, N is the number of unit cells in the system, and we choose $\tau_{\mathrm{A}}=0$ and τ_{B} equal to the vector connecting the two atoms within a unit cell.

The relative orientation of the two layers can be described by a rotation matrix $M(\theta)$ and a translation vector $\mathbf{d}$. Therefore every Bloch wave function in the second layer is related to a Bloch wave function in the first layer by

$$|\Psi_{\mathbf{k}'\alpha}^{(2)}\rangle = |\Psi_{\mathbf{k}\alpha}^{(1)}\rangle \tag{A5}$$

with $|\mathbf{R}+\tau_s\rangle$ in layer 1 replaced by $|\mathbf{R}'+\tau_s'\rangle$ in layer 2, $\mathbf{r}'=M\mathbf{r}+\mathbf{d}$ for all positions and $\mathbf{k}'=M\mathbf{k}$. Using primes to indicate layer 2 variables and invoking the two-center approximation for the interlayer tunneling amplitude,

$$\langle \tau_s+\mathbf{R}|H_{inter}|\tau_s'+\mathbf{R}'\rangle = t(\tau_s+\mathbf{R}-\tau_s'-\mathbf{R}'), \tag{A6}$$

we find that

$$\begin{aligned} T_{\mathbf{k}\mathbf{p}'}^{\alpha\beta} &\equiv \langle \Psi_{\mathbf{k}\alpha}|H_{inter}|\Psi_{\mathbf{p}'\beta}\rangle \\ &= \frac{1}{N}\sum_{ss'} (a_{\mathbf{k}s}^{(\alpha)})^\star a_{\mathbf{p}s'}^{(\beta)} \sum_{\mathbf{R}_1\mathbf{R}_2} e^{-i\mathbf{k}\cdot(\mathbf{R}_1+\tau_s)+i\mathbf{p}\cdot(\mathbf{R}_2'-\mathbf{d}+\tau_{s'}')} \\ &\quad \times t(\mathbf{R}_1+\tau_s-\mathbf{R}_2'-\tau_{s'}'). \end{aligned} \tag{A7}$$

Expression (2) in the main text is obtained by Fourier expanding $t(\mathbf{r})$ and summing over the lattice vectors.

APPENDIX B: VERTEX CORRECTIONS

The general expression for the tunneling current

$$I(\theta,V) = -4eg_s \int \frac{d\omega}{2\pi}[n_2(\omega+eV)-n_1(\omega)] \sum T_{\mathbf{k_0}\mathbf{p_0}}^{\alpha\beta} T_{\mathbf{k_N}\mathbf{p_N}}^{\gamma\delta\star} \overline{\mathrm{Im}\, G_{1\gamma\alpha}^{\mathrm{R}}(\mathbf{k_N},\mathbf{k_0},\omega)\mathrm{Im}\, G_{2\beta\delta}^{\mathrm{R}}(\mathbf{p_0'},\mathbf{p_N'},\omega+eV)} \tag{B1}$$

is obtained using second-order perturbation theory.[34] In Eq. (B1) n_j is the Fermi distribution in layer j, $G_{j\gamma\alpha}^{\mathrm{R}}$ is the retarded Green's function in layer j that correspond to the propagation of a charge carrier from band α to band γ, the rotation angle is θ, and V is the bias voltage. The over line denotes disorder averaging. As in the main text, primed variables are associated with the rotated layer. Since disorder breaks translation invariance, the Green's functions are not diagonal is the momentum representation. When the disorder averages can be performed independently for the two layers, translational invariance is recovered and Eq. (B1) reduces to Eq. (1) of the main text.

We average over disorder using the self-consistent Born approximation in which correlations between the layers appear as a vertex-correction ladder diagram sum (see Fig. 6). For simplicity we assume white-noise disorder and characterize the correlation between the disorder potentials in the two layers by $\gamma=n_i\langle U_1U_2\rangle$, where n_i is the concentration of impurities and U_j is the disorder potential in layer j. For aligned bilayers with short-range tunneling we find that

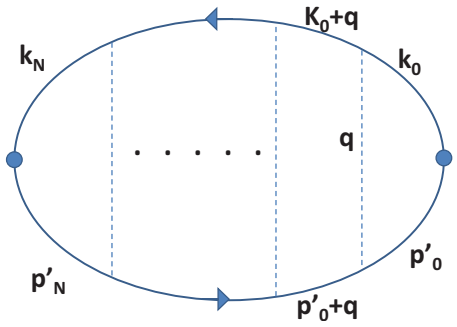

FIG. 6. (Color online) Self-consistent Born approximation. A bubble diagram with ladders.

$$G = \frac{e^2 t^2 \nu_F \tau}{2} \frac{1}{1-\gamma/\beta}, \tag{B2}$$

where $\beta = n_i \langle U_j^2 \rangle$. As evident from Eq. (B2) the tunneling conductance diverges if the disorder potentials of the two layers are perfectly correlated. These strong correlations are likely in a graphene bilayer because of the small distance between the layers. The divergence of G indicates the breakdown of perturbation theory, i.e., it invalidates the incoherent theory we use in this work. A similar scenario arises for tunneling between coupled semiconductor quantum wells[25] when their disorder potentials are strongly correlated.

We now show that vertex corrections are important only at very small values of the rotation angle θ. The physical origin of this behavior is twofold. First, the relevant correlation in the twisted case is between the disorder potential in one layer and a spatially rotated counterpart in the other layer. For any finite-range disorder correlation length, these two disorder potentials are independent making γ in Eq. (B2) considerably smaller. Second, the divergence in the conductance appears due to tunneling between identical states. However, for incommensurate angles the wave vectors of the initial and final states in a tunneling process substantially differ making β in Eq. (B2) considerably larger. In the following paragraphs we explain how this latter behavior is captured in a diagrammatic perturbation-theory description of a disordered system.

We first focus on the tunneling conductance for aligned layers ($\theta=0$). At zero temperature

$$G(\theta) = \frac{2e^2 g_s}{\pi} \sum T^{\alpha\beta}_{\mathbf{k_0 p_0}} T^{\gamma\delta\star}_{\mathbf{k_N p_N'}} \overline{\mathrm{Im}\, G^{\mathrm{R}}_{1\gamma\alpha}(\mathbf{k_N}, \mathbf{k_0}, \epsilon_F) \mathrm{Im}\, G^{\mathrm{R}}_{2\beta\delta}(\mathbf{p_0'}, \mathbf{p_N'}, \epsilon_F)}. \tag{B3}$$

The conservation of crystal momentum in expression (2) for $T^{\alpha\beta}_{\mathbf{kp'}}$ implies that $\mathbf{p_0}=\mathbf{k_0}$ and that $\mathbf{p_N}=\mathbf{k_N}$. For $\epsilon_F \tau > 1$ interband transitions are inhibited so that $\alpha=\gamma$ and $\beta=\delta$. Due to the spinor form of the wave functions each disorder line contributes $[1+\cos(\theta_{k_{j+1}}-\theta_{k_j})]\gamma/2$ to the ladder diagram. To evaluate $\Pi^{(n)}$, the ladder diagram with n disorder lines, we first integrate over the angular variables using

$$\int_0^{2\pi} \frac{d\theta_q}{2\pi} \cos(\theta_{k_1}-\theta_q)\cos(\theta_{k_2}-\theta_q) = \frac{1}{2}\cos(\theta_{k_1}-\theta_{k_2}). \tag{B4}$$

Then using $\mathcal{F}(0)=2\pi\nu_F\tau$, where

$$\mathcal{F}(\mathbf{Q}) = \sum_q G^R_{1\alpha}(q,\omega) G^A_{1\alpha}(\mathbf{q}+\mathbf{Q},\omega), \tag{B5}$$

we integrate over the radial direction. In obtaining $\mathcal{F}(0)$ we have replaced the energy-dependent density of states by ν_F, its value at the Fermi energy. We find that for $n \geq 1$

$$\Pi^{(n)} = G^\mu_1(k_0) G^\nu_2(k_0) \left[1 + \frac{1}{2^{n-1}} \cos(\theta_{k_0} - \theta_{k_N})\right] \times \left(\frac{\gamma}{\beta}\right)^{n-1} \frac{\gamma}{2} G^\mu_1(k_N) G^\nu_2(k_N), \tag{B6}$$

where $\beta = 1/\pi\nu_F\tau$ and $\mu,\nu = R,A$. For $n \geq 2$ the Green's functions in one layer are retarded and those of the other layer are advanced. We now sum $\Pi^{(n)}$ to infinite order in n. While the sum can clearly be carried for a general tunneling matrix element T_{kk} the basic physical idea is more transparent for short-range tunneling. Therefore in the calculations below we assume $T_{kk}=t$ is momentum independent in which case we recover Eq. (B2).

We now address the role played by vertex corrections is twisted bilayers. As in the main text our discussion excludes the vicinity of $\theta = 0°, 60°$ for which $t > 1/\tau$. The procedure outlined above for calculating G can be repeated for any rotation angle θ. For a rotated bilayer it follows from Eq. (2) in the main text that $\mathbf{k_0} - \mathbf{p_0'} = \mathbf{G_2'} - \mathbf{G_1} \equiv \mathbf{Q}$, where $Q \approx |\mathbf{k_D} + \mathbf{G_1}||\theta - \theta_c|$. Expression (B2) can then be used for a rotated bilayer as well if β is replaced by

$$\beta_Q = \beta F(0)/F(Q). \tag{B7}$$

Because $\mathcal{F}$ is a monotonically decreasing function of its argument and because Q is comparable in size to the Dirac momentum $\beta_Q \gg \beta$.

APPENDIX C: THE GEOMETRIC MATRIX

Using a representation of sublattice sites in each layer we find that at the Dirac point

$$\mathcal{T} = \mathcal{T}^{\mathrm{S}} = 2|a| \begin{pmatrix} 1 & 0 \\ 0 & e^{-2i\phi} \end{pmatrix}, \quad \mathcal{T} = \mathcal{T}^{\mathrm{D}} = 2|a| \begin{pmatrix} 1 & 0 \\ 0 & 0 \end{pmatrix}. \quad \text{(C1)}$$

Here $\mathcal{T}^{\mathrm{S}}$ and $\mathcal{T}^{\mathrm{D}}$ correspond, respectively, to intravalley and intervalley rotation angles, and $\phi = 0, \pm 60$ depends on θ_c as explained in the main text. If the hopping amplitude t_q decreases fast enough with momentum so that only the first G shell significantly contribute to the tunneling matrix

$$|a| = 1.5 \frac{t_{\mathbf{k_D}+\mathbf{G_1}}}{\Omega_0}, \quad \text{(C2)}$$

where Ω_0 is the area of a unit cell and $\mathbf{G}_1$ is the wave vector which produces the smallest $\mathbf{q}$ extended-zone Dirac-cone overlap as explained in the text. In our model Eq. (C2) is satisfied for all commensurate angles except for $\theta = 0°, 60°$ for which $|a| = 1.67 t_{\mathbf{k_D}+\mathbf{G_1}}/\Omega_0$. Diagonalizing H_0 yields $E^{\mathrm{S}} = \pm 2|a|$ (both doubly degenerate) and $E^{\mathrm{D}} = 0, 0, \pm 2|a|$. In both cases the energy gap between the top conduction band and bottom valence band is therefore $E_g = 4|a|$.

To find R we assume that T is well approximated by Eq. (C1) for finite momentum states in the vicinity of the Dirac points. We verified this assumption numerically for low densities. In the eigenstate representation

$$T^{\mu\nu}_{kp'} = a^{1\alpha\star}_{k\mu} a^{1\beta}_{k\nu} \mathcal{T}^{\alpha\beta}_{kp'} \delta_{kp'} \quad \text{(C3)}$$

from which Eqs. (16) and (17) readily follow. We then obtain from Eq. (6) that

$$R^{\mathrm{D}} = |a| I \quad \text{(C4)}$$

and

$$R^{\mathrm{S}} = 4|a|^2 \begin{pmatrix} \cos^2\left(\phi - \frac{\theta_c}{2}\right) & \sin^2\left(\phi - \frac{\theta_c}{2}\right) \\ \sin^2\left(\phi - \frac{\theta_c}{2}\right) & \cos^2\left(\phi - \frac{\theta_c}{2}\right) \end{pmatrix}. \quad \text{(C5)}$$

An interesting consequence of Eqs. (4), (C4), and (C5) is that interband resonant conduction (which occurs when the carrier densities in the two layers are opposite) has the same form as its intraband counterpart for intervalley rotation angles. For the interband conduction at intervalley rotation angles the cos function in Eq. (8) should be replaced by a sin.

[1] A. H. Castro Neto, F. Guinea, N. M. R. Peres, K. S. Novoselov, and A. K. Geim, Rev. Mod. Phys. **81**, 109 (2009).
[2] A. K. Geim and A. H. MacDonald, Physics Today **60**, 35 (2007).
[3] J. H. Chen, C. Jang, S. Xiao, M. Ishigami, and M. S. Fuhrer, Nat. Nanotechnol. **3**, 206 (2008).
[4] C. H. Lui, L. Liu, K. F. Mak, G. W. Flynn, and T. F. Heinz, Nature (London) **462**, 339 (2009).
[5] P. W. Sutter, J. I. Flege, and E. A. Sutter, Nature Mater. **7**, 406 (2008).
[6] H. Schmidt, T. Ludtke, P. Barthold, and R. J. Haug, Phys. Rev. B **81**, 121403(R) (2010).
[7] W. A. de Heer, C. Berger, X. Wua, P. N. First, E. H. Conradа, X. Lia, T. Lia, M. Sprinkle, J. Hass, M. L. Sadowski, M. Potemski, and G. Martinez, Solid State Commun. **143**, 92 (2007).
[8] P. N. First, W. A. de Heer, T. Seyller, C. Berger, J. A. Stroscio, and J. Moon, MRS Bull. **35**, 296 (2010).
[9] G. Dobrik, L. Tapaszto, P. Nemes-Incze, Ph. Lambin, and L. P. Biro, Phys. Status Solidi B **247**, 896 (2010).
[10] K. S. Kim, Y. Zhao, H. Jang, S. Y. Lee, J. M. Kim, K. S. Kim, J.-H. Ahn, P. Kim, J.-Y. Choi, and B. H. Hong, Nature (London) **457**, 706 (2009).
[11] D. V. Kosynkin, A. L. Higginbotham, A. Sinitskii, J. R. Lomeda, A. Dimiev, B. K. Price, and J. M. Tour, Nature (London) **458**, 872 (2009).
[12] P. Avouris, Z. Chen, and V. Perebeinos, Nat. Nanotechnol. **2**, 605 (2007).
[13] H.-K. Min and A. H. MacDonald, Phys. Rev. B **77**, 155416 (2008).
[14] Z. Y. Rong and P. Kuiper, Phys. Rev. B **48**, 17427 (1993).
[15] G. Li, A. Luican, J. M. B. Lopes dos Santos, A. H. Castro Neto, A. Reina, J. Kong, and E. Y. Andrei, Nat. Phys. **6**, 109 (2010).
[16] C. Berger, Z. Song, T. Li, X. Li, A. Y. Ogbazghi, R. Feng, Z. Dai, A. N. Marchenkov, E. H. Conrad, P. N. First, and W. A. de Heer, J. Phys. Chem. B **108**, 19912 (2004).
[17] J. Hass, F. Varchon, J. E. Millán-Otoya, M. Sprinkle, N. Sharma, W. A. de Heer, C. Berger, P. N. First, L. Magaud, and E. H. Conrad, Phys. Rev. Lett. **100**, 125504 (2008).
[18] S. Shallcross, S. Sharma, E. Kandelaki, and O. A. Pankratov, Phys. Rev. B **81**, 165105 (2010).
[19] S. Y. Zhou, G.-H. Gweon, and A. Lanzara, Ann. Phys. (N.Y.) **321**, 1730 (2006).
[20] J. M. B. Lopes dos Santos, N. M. R. Peres, and A. H. Castro Neto, Phys. Rev. Lett. **99**, 256802 (2007).
[21] S. Shallcross, S. Sharma, and O. A. Pankratov, Phys. Rev. Lett. **101**, 056803 (2008).
[22] E. McCann and V. I. Falko, Phys. Rev. Lett. **96**, 086805 (2006).
[23] R. Lifshitz, Z. Kristallogr. **222**, 313 (2007).
[24] P. Moses and R. H. McKenzie, Phys. Rev. B **60**, 7998 (1999).
[25] L. Zheng and A. H. MacDonald, Phys. Rev. B **47**, 10619 (1993).
[26] J. P. Eisenstein, T. J. Gramila, L. N. Pfeiffer, and K. W. West, Phys. Rev. B **44**, 6511 (1991), and work cited therein.
[27] D. L. Miller, K. D. Kubista, G. M. Rutter, M. Ruan, W. A. de Heer, P. N. First, and J. A. Stroscio, Science **324**, 924 (2009).
[28] E. J. Mele, Phys. Rev. B **81**, 161405(R) (2010).
[29] S. K. Lyo, Phys. Rev. B **50**, 4965 (1994).
[30] V. M. Pereira, A. H. Castro Neto, and N. M. R. Peres, Phys. Rev. B **80**, 045401 (2009).
[31] L. L. Bonilla and H. T. Grahn, Rep. Prog. Phys. **68**, 577 (2005).
[32] J. S. Bunch *et al.*, Nano Lett. **8**, 2458 (2008).
[33] See, for example, W. A. Harrison, *Elementary Electronic Structure* (World Scientific, Singapore, 1999).
[34] G. D. Mahan, *Many Particle Physics* (Plenum press, New York, 1990).